HIGH POWER LASER
SCIENCE AND ENGINEERING

RESEARCH ARTICLE

Seismic noise contributions to European X-ray free-electron laser bunch arrival time jitter from ocean-generated microseism

Erik Genthe[1], Marie Kristin Czwalinna[1], Björn Lautenschlager[1], Holger Schlarb[1],
Celine Hadziioannou[2], Oliver Gerberding[3], and Katharina-Sophie Isleif[4]

[1] *Deutsches Elektronen-Synchrotron DESY, Hamburg, Germany*

[2] *Institute of Geophysics, University of Hamburg, Hamburg, Germany*

[3] *Institute of Experimental Physics, University of Hamburg, Hamburg, Germany*

[4] *Institute of Automation Technology, Helmut Schmidt University, Hamburg, Germany*

Abstract

Measurements of the bunch arrival times at the European X-ray free-electron laser show noise contributions in the spectral range between 0.05 and 0.5 Hz with peak-to-peak jitter of up to 25 fs. Correlation with distributed acoustic sensing measurements confirms the seismic origin. The seismic noise in this frequency band is known to be ocean-generated microseism. Both primary and secondary ocean-generated microseisms were identified using seismometers and a numerical ocean wave model. Whereas secondary microseism has a strong impact on the bunch arrival time, primary microseism has no notable effect. Rayleigh waves cause the effect, while Love waves have minimal impact. In the presented cases, the noise originates from the North Atlantic and/or the North Sea. The amplitude of the noise depends on the local weather conditions and is much stronger in winter. Ocean-generated microseism is a significant bottleneck that must be addressed to achieve femtosecond bunch arrival time stability in the sub-Hz regime.

Keywords: distributed acoustic sensing; European X-ray free-electron laser; large-scale free-electron laser; microseism; stability

1. Introduction

The European X-ray free-electron laser (XFEL) generates bursts of up to 2700 ultra-short X-ray flashes every 100 ms, with a brilliance that is a billion times greater than conventional X-ray sources. This facility opens up unprecedented research opportunities for scientists and industrial users[1].

The European XFEL facility is located in underground tunnels stretching more than 3 km from the Deutsches Elektronen-Synchrotron (DESY) site in Hamburg. The linear accelerator of the European XFEL delivers electron bunches with high peak currents and high beam energies of up to 17.5 GeV. The electron bunches are sent through up to three undulator beamlines where in the so-called self-amplified spontaneous emission (SASE) process exceptionally short and intense X-ray flashes with laser properties are generated[2].

The European XFEL is an important tool for conducting pump–probe experiments, which are used to study ultrafast phenomena such as atomic motion. In pump–probe experiments, an ultra-short laser pulse excites the sample, followed by another laser pulse that captures the response of the sample. Combining several measurements can provide insights into fast molecular processes, such as biological or chemical reactions that take place within a few femtoseconds[3]. As the demand for higher spatial and temporal resolution in these experiments increases, there is a growing need to improve the temporal stability of the X-ray flashes[4,5].

The European XFEL generates bursts of intense X-ray flashes at a rate of 10 Hz. A window of 600 μs and a maximum intra-burst repetition rate of 4.5 MHz allow one to generate a train of up to 2700 electron bunches per burst[3,6]. With a facility-wide optical synchronisation system and additional beam-based feedback systems, it is ensured that the electron bunches in each 4.5 MHz bucket have a low phase jitter compared to the optical reference. This is referred to as arrival time stability[7]. The present work aims

Correspondence to: E. Genthe, Deutsches Elektronen-Synchrotron DESY, 22607 Hamburg, Germany. Email: erik.genthe@desy.de

to investigate potential improvements of this bunch arrival time stability.

Within the regulation bandwidth of 10–25 kHz, an arrival time stability of less than 10 fs root mean square (rms) is achieved for each of those electron bunches within the burst from which the free-electron laser (FEL) radiation is generated. This jitter performance is continuously monitored with a rolling window of 600 bursts, that is, over 60 s, proving that the reduced noise band of less than 10 fs rms is maintained over days of user operation at the European XFEL[6,8]. Projecting this trend into the future, the next goal is to reach a level of 1 fs rms by 2030.

Five main areas for reducing bunch arrival time jitter have been identified[9]. The first is a reduction of the fast electron bunch jitter observed in the frequency range between 1 kHz and 1 MHz. This is primarily a matter of monitor resolution; therefore, a new generation of bunch arrival time monitors (BAMs) is under development. Secondly, considerable timing variations stem from the pump–probe laser system, which can be measured and corrected by laser-pulse arrival time monitors (LAMs) and fast feedback mechanisms[6]. The third is to address slow drifts (<0.01 Hz) that occur in the optical reference system due to environmental changes such as relative humidity, air pressure and temperature. The fourth concerns very slow drifts that are caused by tidal effects at about 0.02 mHz[8]. Finally, the fifth is a prominent noise peak often observed in the 0.05–0.5 Hz frequency band. This disturbance has varying intensity and the frequency spectrum varies within the 0.05–0.5 Hz band. Similar characteristics have been observed for ocean-generated microseism, which are seismic waves that are generated by the interaction of ocean waves with Earth's crust[10,11,12]. In this work we investigate this observed noise band and its relation to ocean-generated microseism, and explore ways to mitigate its impact on the bunch arrival time stability, which is necessary to reach the 1 fs goal for experiments at the European XFEL.

To investigate the impact of ocean-generated microseism on the accelerator, three measurement systems have been used. First are the BAMs, which measure, in specific

sections, deviations from the expected arrival time compared to the optical reference[1] (Section 2.4). Second is distributed acoustic sensing (DAS)[13], which measures the strain of an optical fibre, resolved in time and space (Section 2.3). The fibre runs through the tunnel and is therefore expected to measure the strain of the tunnel. Third is a seismometer, which is placed at the injector of the European XFEL (Section 2.5). The seismometer measures ground velocity in all three axes (north, east, vertical) and allows for more in depth analysis of seismic wave properties.

2. Methods

This section describes the setups and techniques used for this research, starting with the DAS methods, followed by BAM signal processing, seismometer setup and Wavewatch III numerical simulation data acquisition.

2.1. DAS setup

DAS allows seismic signals to be recorded along tens of kilometres of optical fibre with high spatial resolution and over a wide frequency range from sub-millihertz up to 50 kHz. A DAS interrogator sends laser pulses through an optical fibre and analyses the phase of the backscattered light. Vibrations strain the fibre, causing changes in the backscatter that are detected at specific points, called channels. The gauge length defines the length of the fibre segment over which these changes are measured[14].

The DAS interrogator used in this study is called iDAS™ and was developed by Silixa Ltd and provided by the WAVE collaboration. The WAVE collaboration investigates and designs a seismic and geo-acoustic measurement network in and around Science City Hamburg Bahrenfeld. WAVE is an infrastructure for geophysics, physics and especially for large-scale research facilities[15].

A total of 12,608 m of optical fibres, located on the DESY campus and in the European XFEL, are connected to the DAS interrogator (Figure 1). The fibre runs from
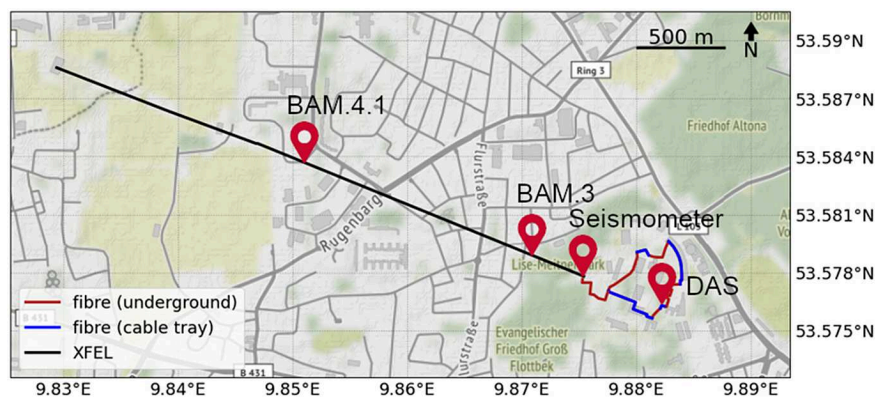
Figure 1. Map illustrating the location of the seismometer and the path of the fibre connected to the DAS instrument (courtesy of Sandy Croatto).

Building 35, where the DAS instrument was located, to the European XFEL: from the injector building (XSIN), through the main linear accelerator tunnel (XTL), through the undulator tunnels (XTD2 and XTD9) into the experimental hall. There the fibre is spliced to another fibre of the same cable so that the pulses travel back the same way to Building 35. There, another cable is connected, which runs through cable ducts across large parts of the DESY campus, then alongside the PETRA III tunnel and back into Building 35 (Figure 1). Here again, two fibres of the cable are spliced together so that the pulses travel back the same way across the DESY campus. The mapping of relevant locations to DAS channel numbers is described in Section 2.2.

Within the fibre loop connected to the DAS interrogator, different optical single mode fibres (SMFs) are used. In the European XFEL tunnel from the injector building (XSE) through the linear accelerator to the undulator tunnel (XSE), an FTTx A-DQ(ZN)2Y cable with a G.657.A fibre is used. Elsewhere, a cable with the identifier U-DQ(ZN)BH and fibre type 652.D is used. Both cables are 'loose tube', meaning that the fibre is intended to slide inside the cable, which can affect high spatial resolution DAS measurements. These fibres are low bend loss SMF fibres with a damping of less than or equal to 0.21 dB/km at 1550 nm.

Configuration parameters of DAS system are as follows:

- sampling rate: 1000 Hz;

- gauge length: 10 m;

- channel spacing: 1 m;

- number of channels: 12,608;

- bit depth of written data: 16-bit integer;

- data rate: 25.2 MB/s = 2179 GB/day.

2.2. Georeferencing of DAS data

Georeferencing is the process of assigning geographic locations, such as geo-coordinates, to recorded acoustic events.

To determine the locations of BAM.3 and BAM.4.1, we tapped the tunnel floor next to each BAM with a rubber hammer while the DAS instrument was performing measurements. These hammer taps can be identified in the data. To make the hammer taps visible, the strain data was high-pass filtered before integration at 100 Hz using discrete Fourier transform (DFT). The rms strain is expected to be strongest at the channel closest to the hammer impact, which is next to the respective BAM. BAM.3 is at channel 1445 and BAM.4.1 is at channel 2955. This corresponds to a distance of 1510 m.

2.3. Signal processing of DAS data

DAS data was captured from 9 December 2022 to 9 March 2023 (89 days) and from 25 May 2023 to 12 October 2023 (140 days). The resulting total amount of data is approximately 460 TB.

A reduced version of the full DAS dataset is required to make long-term analyses feasible. Choosing an appropriate downsampling method is crucial to prevent signal distortion and aliasing. Among the methods considered, average downsampling was selected for its ease of implementation, computational efficiency and consistent frequency spectrum, making it suitable for analysing ocean-generated microseisms in the 0.05–0.5 Hz range.

To calculate the average strain of the European XFEL between BAM.3 and BAM.4.1 (Figure 1), the corresponding channels have been averaged.

The relative deviation of bunch arrival times measured by the two BAMs is proportional to the strain of the tunnel section if the given signal is of seismic origin. Our particular DAS interrogator measures strain rate ($\frac{nm}{m \cdot s}$), which we integrate in time to obtain strain data. This reduces high-frequency noise but greatly amplifies temperature drifts.

DAS measurements are sensitive to temperature variations of both the instrument and the fibre. BAM measurements, on the other hand, are not sensitive to temperature-induced changes and therefore it is necessary to remove the temperature drifts from the DAS signal, which is done by high-pass filtering. Temperature drifts are typically many orders of magnitude stronger than ocean-generated microseism in strain data and have orders of magnitude lower frequencies[16]. DFT is used to remove temperature drifts. This method produces a sharp frequency cutoff. Strong spectral smearing effects can occur due to the large magnitude of temperature drifts, which is avoided by applying this method prior to integration. The selected cutoff frequency is 0.05 Hz.

2.4. Signal processing of BAM data

After extracting the data from the data acquisition system (DAQ) of the European XFEL[17], the samples (bunch trains) are sorted by their unique bunch-train-id. The sampling rate is 10 Hz, since the European XFEL accelerates 10 bunch trains per second. Around 2% of the samples are missing and substituted using cubic spline interpolation.

Ocean-generated microseism strains the tunnel. Strain is proportional to the relative bunch arrival delay between two points in the accelerator tunnel. This is retrieved by calculating the difference between the arrival times at two BAMs. It is important to note that from a beam dynamics point of view, no relative deviations in the measured arrival time compared to the optical reference are actually expected between BAM.3 and BAM.4.1, as there is only a drift section between these two measurement points[8].

Finally, an interval of bunches per bunch train is selected for averaging. The European XFEL produces bunch trains at a rate of 10 Hz and, within one bunch train, there can be up to 2700 bunches. Averaging as many bunches as possible

reduces the noise level. Only bunches from a stabilized beam region are used to achieve low noise results. A stabilized beam region can be identified by its low arrival time jitter within a bunch train. The accelerator's feedback system needs some time to achieve sufficient stability and suffers from the transition to the next beam region. Therefore, the first and last 50 bunches within a beam region are not used[8].

2.5. Seismometer setup

The Güralp Systems CMG-3TD is a three-component digital broadband seismometer. In the ocean-generated microseism frequency band from 0.05 to 0.5 Hz, the attenuation of the seismometer is close to 0 dB.

The seismometer is located in the seventh underground level at NN+7.6 m (29.4 m below the surface) in the injector building of the European XFEL (Figure 1). The seismometer stands on a concrete floor about 2 m thick. Below the floor is the secondary injector tunnel, and further below is the primary injector tunnel that is in use today. The heavy concrete plate can absorb much of the higher frequency noise, creating a quiet measurement situation, which helps to measure lower frequency motions such as ocean-generated microseism.

2.6. Acquisition of numerical ocean wave data from the Wavewatch III model

The simulation results were retrieved from the Wavewatch III model, a numerical wave model designed to simulate and forecast ocean waves. The model provides various wave parameters such as wave height, wave direction and wave period on a global scale[18]. It is widely used in oceanography, marine forecasting and climate research[19].

3. Results

This section presents the results of the data analyses conducted. It covers four sections: a year-long overview of microseisms using DAS data, evidence linking the observed noise to seismic origins by comparing BAM and DAS data, an exploration of the generation mechanism of the ocean-generated microseism using seismometer data and a comparison of seismometer data with Wavewatch III simulations to identify the source of the microseisms.

3.1. Long-term characteristics

Ocean-generated microseism has a strong seasonal dependence[20,21]. To search for seasonal variation in the DAS measurements, the whole DAS dataset, including measurements from December 2022 to September 2023 (inclusive) was visualized. As a first step, the complete 460 TB of DAS data

was downsampled by averaging to a frequency of 10 Hz and a spatial pixel size of 10 m, resulting in a dataset of 460 GB, as explained in Section 2.3. Exactly those channels that correspond to the tunnel section from BAM.3 to BAM.4.1, as explained in Section 2.2, are selected and averaged to a one-dimensional time series. In order to have units consistent with the other experiments, the strain rate data is integrated to strain. The resulting measure represents the average strain along the relevant tunnel section. From this prepared data the spectral density is calculated using sliding windows with a size of $2^{15} = 32,768$ samples (3276.8 s). Spectral smearing was reduced by prior multiplication with a Hanning window function.

The spectral density data is visualized in several ways. Figure 2 shows the full spectrogram. For the visualisation of the spectrogram, nearest-neighbour interpolation was used. Figure 3 shows the rms of the ocean-generated microseism spectrum (from 0.05 to 0.5 Hz). It contains annotations for all earthquakes worldwide with a magnitude of six or greater. The earthquakes are retrieved from the United States Geological Survey (USGS) earthquake catalogue[22].

In some periods DAS measurement data is missing. During winter the instrument was set up and in March, April and early May the DAS was used for another experiment.

Ocean-generated microseism depends on weather conditions. In the North Atlantic and North Sea, winds are significantly stronger in winter than in summer[23]. The DAS measures a strain of 0.35 nm/m rms in December, while it is only 0.06 nm/m rms in June, which is a factor of six in difference (Figure 2). From Section 3.2 we know the relation between strain and bunch arrival time. Therefore, the impact corresponds to 3.5 fs rms in December and 0.6 fs rms in June. It is important to note that this is the rms over the whole month. Within a month there is a high variation of the strain and bunch arrival time stability (Figure 3). As a consequence, the peak effects are much higher, as shown in Section 3.2. Finally, there is significantly stronger ocean-generated microseism during winter and therefore a better bunch arrival time stability can be expected during the summer.

Earthquakes release a burst of energy in a broad frequency range[24] and are therefore visible in the ocean-generated microseism frequency band. Figure 3 reveals that the spikes in the ocean-generated microseism spectrum are caused by earthquakes. In Figure 2, earthquakes cause horizontal stripes, due to their broad frequency spectrum, high intensity and short duration. The peak on 9 September was caused by the prominent 6.8 magnitude earthquake in Morocco. This quake caused exceptionally strong strain at the European XFEL because of its magnitude and its relative proximity. All earthquakes in September with a magnitude of 6 or greater are annotated in Figure 3. This covers most of the peaks. On closer inspection, unannotated spikes remain that are stronger than some annotated spikes. These could be
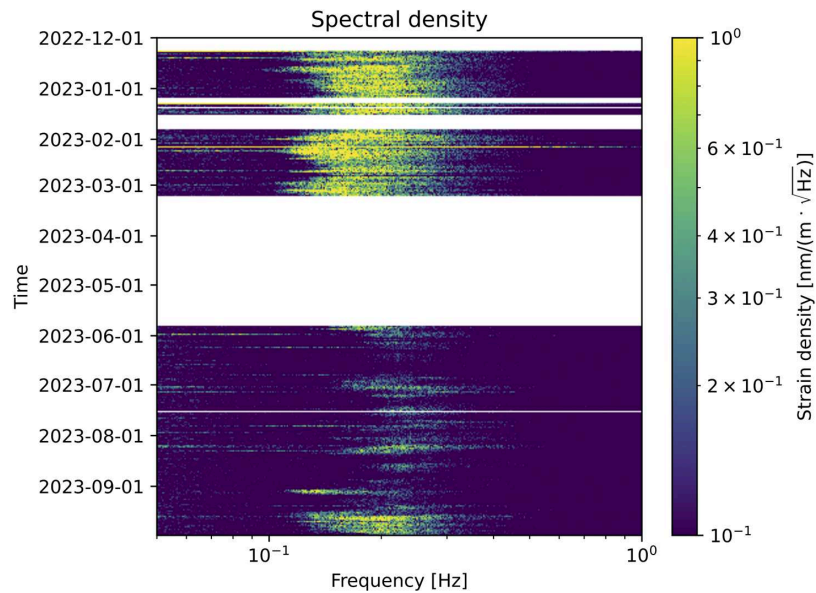
Figure 2. Spectrogram made from the entire DAS dataset. There is a prominent seasonal amplitude contrast between summer and winter. The yellow/green horizontal stripes are caused by earthquakes due to their broad frequency spectrum, high intensity and short duration. Blank areas indicate periods with no data available.
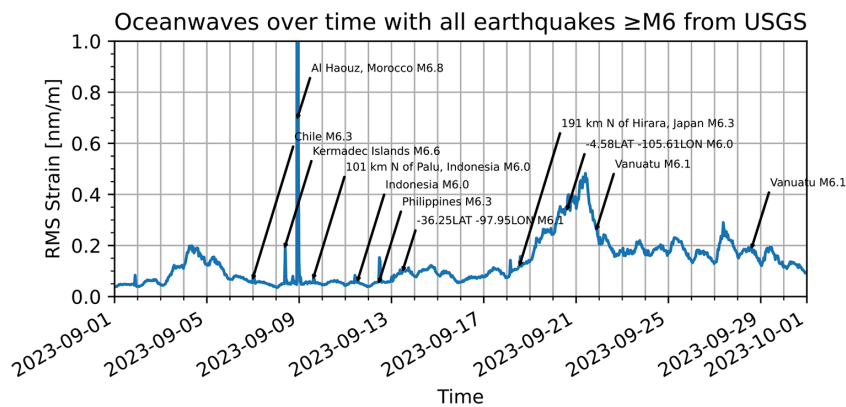
Figure 3. The rms of the ocean-generated microseism frequency band [0.05 Hz, 0.5 Hz] in September 2023, based on the data shown in Figure 2. It can be seen that earthquakes have frequency components within the ocean-generated microseism frequencies. The spikes without annotations are most likely caused by lower-magnitude earthquakes.

weaker earthquakes that are closer to the European XFEL and/or better match the selected frequency range.

In September, data was collected from as many instruments as possible to allow for a comparison between independent measurements. Figure 3 shows that there were two periods with strong signals at the ocean wave frequencies. These are 4 September, with weaker and very low-frequency signals, and 21 September, with stronger and higher frequency signals. These two periods are analysed in further detail in this section, incorporating measurements from DAS, BAMs and seismometers.

### 3.2. Comparison of bunch arrival time with physical strain (DAS)

Strong bunch arrival time jitter can be observed at the European XFEL within the frequency range from 0.05 to

0.5 Hz (Figure 4). The analysis reveals that the observed bunch arrival time jitter in this frequency range can also be accurately measured with the DAS instrument, indicating its seismic origin.

By averaging the measured arrival times of several bunches, it is possible to significantly reduce the BAM measurement noise so that even weak ocean-generated microseism can be detected. It is important that only bunches within a stabilized beam region are used. In the beam regions without active arrival time stabilisation, we observe much larger contributions in the less than 10 Hz range, and up to 25 fs rms (over 10 s), which mask the ocean wave components. It is only with active arrival time stabilisation, which synchronizes the electron bunches to the optical reference, that such interference signals, which cannot be intercepted with synchronisation, can be resolved metrologically at all[6,8]. How the bunches are selected is described in Section 2.4.
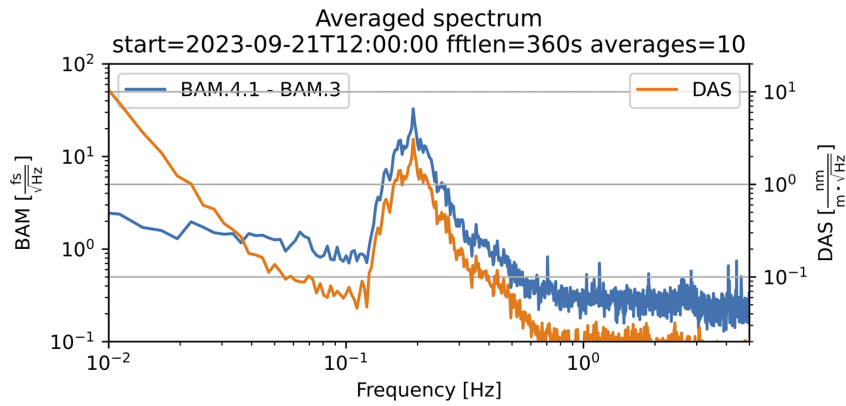
Figure 4. Comparison of BAM and DAS frequency spectra for 1 h of data. For this visualization, the DAS data is not high-pass filtered. The scales are aligned, so that 1 nm/m corresponds to 5 fs as in Equation (1).
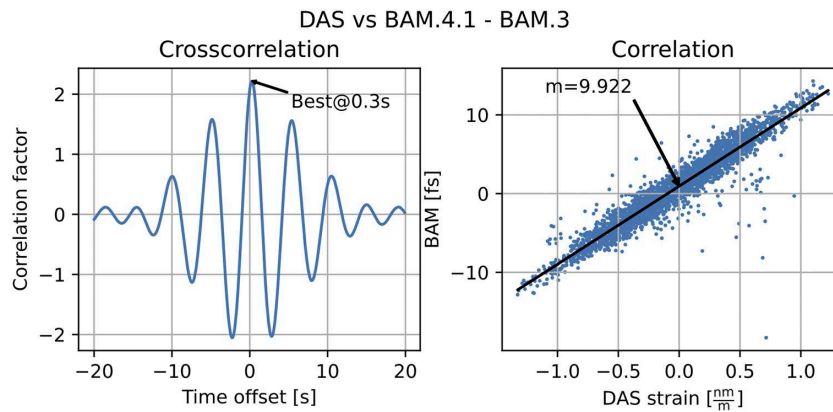
Figure 5. Correlation of the BAM with DAS data using a time window of 300 s (3000 samples each). Firstly, the cross-correlation (shown on the left) is calculated to correct for time offsets. Secondly, the correlation plot (shown on the right) was created and linear regression was performed. The correlation factor resulting from the regression is 9.922 fs/(nm/m).

In order to obtain a measure from BAMs that can be compared with strain measurements from DAS, the difference between the averaged measurements from two different BAMs is calculated. The measured strain is supposed to be proportional to the difference in relative bunch arrival times.

The seismically induced difference in relative bunch arrival times between these two BAMs is expected to be directly proportional to the accelerator tunnel strain between these two BAMs, which is equal to the strain of the optical fibre. The expected proportional factor depends only on the distance between the BAMs d and the velocity of the electrons c, which is very close to the speed of light in vacuum. BAM.3 is located at 414 m and BAM.4.1 at 1932 m along the European XFEL, so the distance is $1932\,\text{m} - 414\,\text{m} = 1518\,\text{m}$. Equation (1) shows that a change of 1 nm/m in strain is expected to result in a delay of about 5 fs in the bunch arrival time:

$$t = \frac{e \cdot d}{c} \Rightarrow t = \frac{1\,\frac{\text{nm}}{\text{m}} \cdot (1932\,\text{m} - 414\,\text{m})}{299{,}792{,}458\,\frac{\text{m}}{\text{s}}} \approx 5.064\,\text{fs}. \quad (1)$$

Using the correlation factor of Equation (1), the frequency spectra of the measured difference of relative bunch arrival times and the DAS data can be compared. Figure 4 shows the frequency spectra of both measurements without high-pass filtering. Strong low-frequency signals are caused by the temperature sensitivity of DAS and are not visible in the BAM spectrum. At higher frequencies, the spectra are in good agreement. The ocean-generated microseism peak is visible at 0.18 Hz. The data remain in their respective units, fs and nm/m, but the scales are shifted so that 1 nm/m corresponds to 5 fs, as derived from Equation (1). Therefore, the scales are aligned such that the signal amplitudes are supposed to match, but the comparison reveals a discrepancy.

Equation (1) derives the expected linear correlation factor. Despite that, the actual correlation factor for this measurement is calculated as shown in Figure 5. Firstly, the cross-correlation is calculated to find and compensate for offsets in time. Secondly, the correlation factor is calculated using linear regression. The correlation factor resulting from the linear regression is 9.922 fs/(nm/m), which is 96% higher than the expected factor of 5.064 fs/(nm/m)
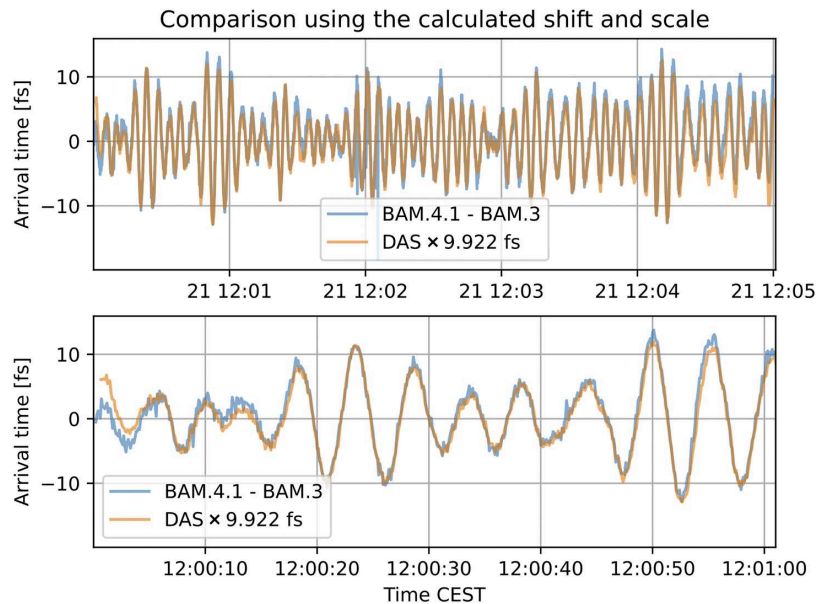
Figure 6. Comparison of the BAM and DAS data using the calculated shifting and scaling factors. The lower figure is a zoomed version of the upper one. The DAS data is scaled with the correlation factor calculated by linear regression, as shown in Figure 5. Both signals are dominated by ocean-generated microseism.

(Equation (1)). The possible sources of this discrepancy are discussed in Section 4. After scaling the DAS data by the factor 9.922 fs/(nm/m), the BAM data correlates very well with the DAS measurements (Figure 6). Apart from the discrepancy in the linear correlation factor, the very good correlation proves that the noise in the 0.05–0.5 Hz frequency band has a seismic origin.

3.3. Wave type based on seismometer data

In this section, seismometer data is used, exploiting the three components (north, east, vertical), to show the types of seismic waves and the mechanisms involved in their generation.

Figure 7 shows a comparison of the three components of the seismometer: north, east and vertical. One hour of data, recorded at 200 Hz sampling rate, was divided into 10 equally sized parts. The power spectral density was calculated for each part and finally averaged to a single power spectral density. A Hanning window function was applied and the window size used for the DFT was 72,000 samples, which corresponds to 360 s. This process was performed individually for each of the three components: north, east and vertical.

Each spectrum shows two distinct peaks: at 0.065 and 0.13 Hz on 4 September and at 0.08 and 0.18 Hz on 21 September. The latter matches the strong ocean-generated microseism peak visible in the DAS and BAM data (Figure 4). Unlike here in the seismometer data, the BAM and DAS measurements do not show the lower frequency peak at 0.065 Hz.

The two peaks correspond to the primary (lower frequency peak) and secondary (higher frequency peak) ocean-generated microseism mechanisms. There are four observations that point in this direction, as those are properties typical for ocean-generated microseism[10–12,25].

- The peaks differ by almost a factor of two.

- The higher frequency peak is much stronger than the lower frequency peak.

- The clouds in the spectrogram around the given frequencies have a very similar shape and occur at the same time (Figure 7).

- For the lower frequency peak, the vertical component is much weaker than the horizontal components, while at the higher frequency peak, the three components have the same amplitude. This has already been observed by Ref. [11] for primary and secondary microseism, respectively.

There are four main types of seismic waves: primary, secondary, Love and Rayleigh waves. Primary and secondary waves are body waves and must not be confused with primary and secondary microseism. Love and Rayleigh waves are surface waves[25]. Which types of waves are included in the ocean-generated microseism at the European XFEL? In general, ocean-generated microseism consists mainly of surface waves (Love and Rayleigh waves)[21]. Love and Rayleigh waves can be identified by comparing the ratio of vertical to horizontal components. While Rayleigh waves are expected to have equal amplitudes horizontally and vertically, Love waves have no vertical component at all. Figure 7 shows
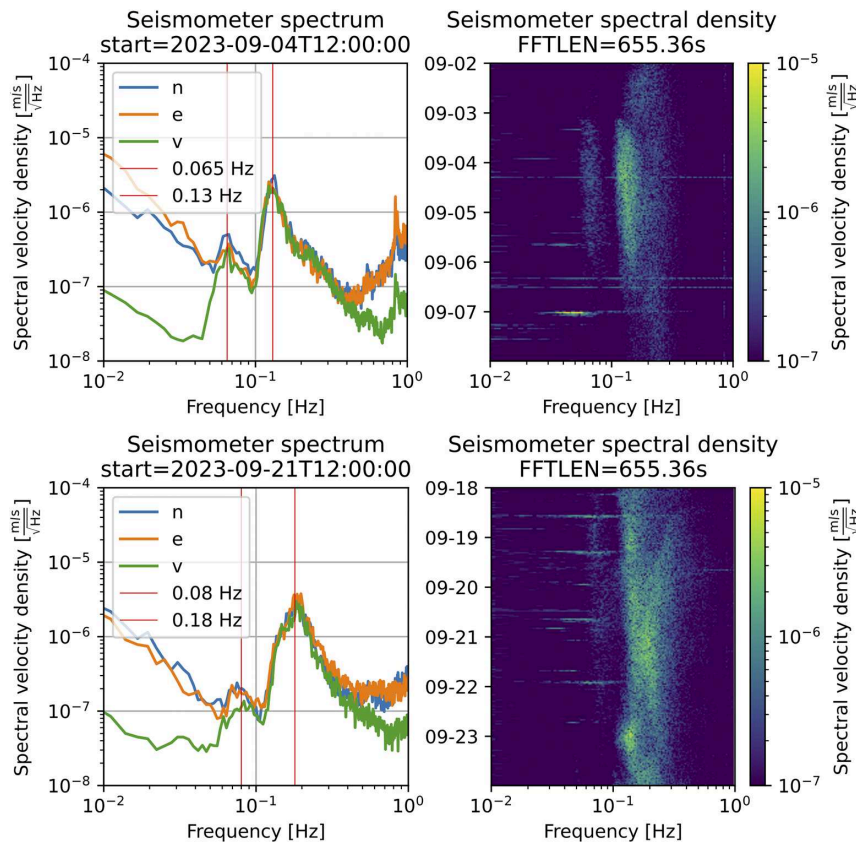
Figure 7. Seismometer data of two periods in September with strong microseism: the days around 4 and 21 September 2023. On the left is an averaged spectral density of each component (north, east, vertical). The spectrogram on the right shows the vertical component over a period of several days.

that at the lower frequency peaks (primary microseism) the vertical component is much weaker, suggesting a higher proportion of Love waves, while at the higher frequency peak (secondary microseism) all three components have almost equal amplitudes, suggesting a high proportion of Rayleigh waves. This is in agreement with seismic observations in northern Europe[11,21].

3.4. Comparison with numerical ocean wave model Wavewatch III

The aim of this section is to find the origin of the ocean-generated microseism observed at the European XFEL. For this purpose, the seismometer measurements of Section 3.3 are compared with the ocean wave heights and periods in the North Sea and the North Atlantic, which are obtained from the numerical model Wavewatch III, developed by the National Oceanic and Atmospheric Administration (NOAA) to forecast and calculate ocean waves[18].

For this section, there are two important metrics: wave height and wave frequency. Wave height refers to the average height of the highest third of waves at a particular point in the ocean. Wave frequency refers to the inverse of the peak wave period. The peak wave period is the period of the most energetic waves passing through a particular point

in the ocean. This corresponds to the group of waves that contributes the most energy. This results in a sudden jump each time a different group of waves becomes the strongest. Often these jumps represent swell fronts, but sometimes they are just artefacts of the ranking mechanism[26]. All ocean wave frequencies and periods given below are taken from the Wavewatch III numerical model.

On 4 September 2023, strong ocean waves with heights of up to 7 m and frequencies of around 0.08 Hz were present in the Azores. In the North Atlantic, near the Shetland Islands, strong ocean waves with significant wave heights of up to 5 m and frequencies of around 0.07 Hz have been calculated. In the North Sea, ocean waves are much smaller, with significant wave heights below 1.5 m and frequencies around 0.065 Hz. In the Baltic Sea, frequencies are around 0.25 Hz and significant wave heights are only around 0.5 m. Therefore, no significant impact is expected from the Baltic Sea. The frequency of the primary microseism peak in the seismometer data matches very well with the frequencies of ocean waves in the North Atlantic near the Shetland Islands and the North Sea. It seems more likely that the primary microseism originates near the Shetland Islands, as the significant wave heights are much larger. In addition, the ocean waves are directed towards the Shetland Islands, and near the Shetland Islands there is a strong slope of the seabed

from 200 m down, whereas the North Sea is much shallower and has less sloping. A sloping seabed is important for the generation of primary microseism[12].

On 21 September 2023, at the location with the highest significant wave height of 7.5 m in the North Atlantic, ocean wave frequencies are around 0.08 Hz. The same frequency dominates the North Sea but with smaller significant wave heights below 4 m. These frequencies perfectly match the primary microseism peak in the seismometer data and would also explain the strong secondary microseism peak at 0.18 Hz, because secondary microseism has twice the frequency of primary microseism[10,25].

Only close to the coast are the ocean wave frequencies higher. In particular, in the German Bight with smaller significant wave heights below 2.5 m, ocean waves have frequencies up to 0.3 Hz. It is possible that these ocean waves in the German Bight are visible on the seismometer data as local primary microseism and could explain the strong noise floor in Figure 7 at frequencies above the secondary microseism peak. Local primary microseism can only be observed close to the coast and the German Bight is only 100 km from the European XFEL and the seismometer. Local primary microseism is explained in detail in Ref. [11].

In these two cases in September, the microseism peaks measured at the European XFEL match the wave frequencies at the locations of the strongest ocean waves in the North Atlantic. However, it remains unclear from which of the two seas the microseism originated, as similar wave frequencies were present in the North Sea and the North Atlantic in the specific cases.

4. Discussion

This paper demonstrates that ocean-generated microseism significantly impacts the bunch arrival time stability of the European XFEL in the frequency range of 0.05–0.5 Hz. Both primary and secondary ocean-generated microseisms were identified using seismometers and a numerical reference model. Secondary microseism has a strong impact on the bunch arrival time, whereas primary microseism has no notable effect. In the presented cases, the seismic noise originates from the North Atlantic and/or the North Sea. The amplitude of the noise depends on the weather conditions in the North Sea and the North Atlantic and is much stronger in winter, when generally higher wind speeds and the regular occurrence of storm systems result in increased ocean wave activity and thus stronger microseism. In summary, this study shows that ocean-generated microseism is a significant bottleneck that must be addressed to achieve femtosecond bunch arrival time stability.

The BAM and DAS measurements correlate strongly, as shown in Section 3.2. Only downsampling and high-pass filtering of the DAS signal are required to match the sampling frequency and remove temperature drifts. By using only a

few simple signal processing methods, the analysis retains high significance and a low probability of error. Overall, the comparison shown in Section 3.2 proves that the given bunch arrival time jitter is caused by seismic activity, which must be addressed to achieve femtosecond bunch arrival time stability.

The correlation factor resulting from the regression is 96% higher than the expected factor from Equation (1). Apart from the scaling, the BAM data correlates strongly with the DAS measurements, as shown in Figures 5 and 6. The origin of this discrepancy factor remains unclear. It seems possible that it is caused by the properties of the DAS cable and its coupling to the tunnel[27].

Earthquakes, but also other additional disturbances like car traffic, can interfere with ocean-generated microseism. Earthquakes occur irregularly, last from minutes to hours, and their amplitudes can be orders of magnitude larger than those of ocean-generated microseism. The frequency spectrum is typically very broad and can intersect with the ocean-generated microseism frequency range[25]. Cars, however, only generate signals on channels in their immediate vicinity. Typically, some channels are stretched while others are compressed at the same time so that the sum of the car traffic signals over all channels is approximately zero. This makes it easy to remove car traffic from ocean-generated microseism signals, by calculating the average of multiple channels.

The identified primary and secondary microseisms have a similar shape in the spectrogram (Figure 7), suggesting that they originate from the same event, location and time. The shape of the seismometer spectra agrees well with previous analyses reported by Refs. [11, 25, 28], where primary and secondary microseism peaks were observed at similar frequencies and amplitudes. There is also a similarity among their overall spectral shapes and in the ratios of vertical to horizontal components. Another shape is visible in the spectrogram of 4 September (Figure 7) at frequencies above 0.3 Hz, which has not been identified. This may be ocean-generated microseism from another event at another location, but it remains unclarified. Unfortunately, it is difficult to identify because it is overlapped by the strong secondary microseism.

The seismometer measurements show a strong secondary and a weak primary microseism peak, but in the BAM and DAS measurements, only the secondary microseism peak is visible. One reason is that the primary microseism is so weak that it is below or just above the noise floor in the BAM and DAS measurements. In addition, the primary microseism has a lower proportion of Rayleigh waves and a higher proportion of Love waves, as discussed in Section 3.3 and observed by Ref. [11]. Love waves induce mainly shear and only little strain[25]. BAM and DAS measurements only measure strain and cannot measure shear. Therefore, the influence of primary microseism on BAM and DAS measurements is even smaller. As a result, primary microseism

is not visible in the BAM and DAS measurements, and has a negligible effect on the bunch arrival time jitter.

5. Conclusion

Ocean-generated microseism significantly impacts the bunch arrival time of the European XFEL within the 0.05–0.5 Hz frequency range. The identification of both primary and secondary ocean-generated microseisms using a seismometer and a numerical reference model reveals that while secondary microseism exerts a strong influence on the bunch arrival time, primary microseism has no notable effect. This can be attributed to the smaller amplitudes of primary microseism and its higher Love wave to Rayleigh wave ratio. Rayleigh waves are the main source of bunch arrival time jitter, whereas Love waves have a negligible influence. In the presented cases, the noise originates from the North Atlantic and/or the North Sea, and the amplitude of the noise is weather dependent, being particularly stronger in winter. As a result, generally better bunch arrival time stability can be expected during summer.

The European XFEL enables cutting-edge precision in scientific experiments. To capture interactions of matter at the smallest scales, it is essential to manage any noise that influences the bunch arrival times. In conclusion, this study shows that ocean-generated microseism is a significant bottleneck that must be addressed to achieve femtosecond bunch arrival time stability.

This work potentially improves future timing resolution in pump–probe experiments. BAMs can detect the arrival of electron bunches, but not the final X-ray FEL photon pulses at the experiment. The DAS system can be used to predict ocean-generated arrival time delays of the FEL photon pulses propagating from the undulator to the experimental hall where the pump experiment is carried out. These measurements could then be used to correct the temporal alignment between the X-ray photons and the synchronized pump–probe lasers, either by post-sorting of data or, in real time, using a feedback control loop.

References

1. W. Decking, S. Abeghyan, P. Abramian, A. Abramsky, A. Aguirre, C. Albrecht, P. Alou, M. Altarelli, P. Altmann, K. Amyan, V. Anashin, E. Apostolov, K. Appel, D. Auguste, V. Ayvazyan, S. Baark, F. Babies, N. Baboi, P. Bak, V. Balandin, R. Baldinger, B. Baranasic, S. Barbanotti, O. Belikov, V. Belokurov, L. Belova, V. Belyakov, S. Berry, M. Bertucci, B. Beutner, A. Block, M. Blöcher, T. Böckmann, C. Bohm, M. Böhnert, V. Bondar, E. Bondarchuk, M. Bonezzi, P. Borowiec, C. Bösch, U. Bösenberg, A. Bosotti, R. Böspflug, M. Bousonville, E. Boyd, Y. Bozhko, A. Brand, J. Branlard, S. Briechle, F. Brinker, S. Brinker, R. Brinkmann, S. Brockhauser, O. Brovko, H. Brück, A. Brüdgam, L. Butkowski, T. Büttner, J. Calero, E. Castro-Carballo, G. Cattalanotto, J. Charrier, J. Chen, A. Cherepenko, V. Cheskidov, M. Chiodini, A. Chong, S. Choroba, M. Chorowski, D. Churanov, W. Cichalewski, M. Clausen, W. Clement, C. Cloué, J. A. Cobos, N. Coppola, S. Cunis, K. Czuba, M. Czwalinna, B. D'Almagne, J. Dammann, H. Danared, A. de Zubiaurre Wagner, A. Delfs, T. Delfs, F. Dietrich, T. Dietrich, M. Dohlus, M. Dommach, A. Donat, X. Dong, N. Doynikov, M. Dressel, M. Duda, P. Duda, H. Eckoldt, W. Ehsan, J. Eidam, F. Eints, C. Engling, U. Englisch, A. Ermakov, K. Escherich, J. Eschke, E. Saldin, M. Faesing, A. Fallou, M. Felber, M. Fenner, B. Fernandes, J. M. Fernández, S. Feuker, K. Filippakopoulos, K. Floettmann, V. Fogel, M. Fontaine, A. Francés, I. Freijo Martin, W. Freund, T. Freyermuth, M. Friedland, L. Fröhlich, M. Fusetti, J. Fydrych, A. Gallas, O. García, L. Garcia-Tabares, G. Geloni, N. Gerasimova, C. Gerth, P. Geßler, V. Gharibyan, M. Gloor, J. Głowinkowski, A. Goessel, Z. Gołebiewski, N. Golubeva, W. Grabowski, W. Graeff, A. Grebentsov, M. Grecki, T. Grevsmuehl, M. Gross, U. Grosse-Wortmann, J. Grünert, S. Grunewald, P. Grzegory, G. Feng, H. Guler, G. Gusev, J. L. Gutierrez, L. Hagge, M. Hamberg, R. Hanneken, E. Harms, I. Hartl, A. Hauberg, S. Hauf, J. Hauschildt, J. Hauser, J. Havlicek, A. Hedqvist, N. Heidbrook, F. Hellberg, D. Henning, O. Hensler, T. Hermann, A. Hidvégi, M. Hierholzer, H. Hintz, F. Hoffmann, M. Hoffmann, M. Hoffmann, Y. Holler, M. Hüning, A. Ignatenko, M. Ilchen, A. Iluk, J. Iversen, M. Izquierdo, L. Jachmann, N. Jardon, U. Jastrow, K. Jensch, J. Jensen, M. Jezabek, M. Jidda, H. Jin, N. Johansson, R. Jonas, W. Kaabi, D. Kaefer, R. Kammering, H. Kapitza, S. Karabekyan, S. Karstensen, K. Kasprzak, V. Katalev, D. Keese, B. Keil, M. Kholopov, M. Killenberger, B. Kitaev, Y. Klimchenko, R. Klos, L. Knebel, A. Koch, M. Koepke, S. Köhler, W. Köhler, N. Kohlstrunk, Z. Konopkova, A. Konstantinov, W. Kook, W. Koprek, M. Körfer, O. Korth, A. Kosarev, K. Kosiński, D. Kostin, Y. Kot, A. Kotarba, T. Kozak, V. Kozak, R. Kramert, M. Krasilnikov, A. Krasnov, B. Krause, L. Kravchuk, O. Krebs, R. Kretschmer, J. Kreutzkamp, O. Kröplin, K. Krzysik, G. Kube, H. Kuehn, N. Kujala, V. Kulikov, V. Kuzminych, D. La Civita, M. Lacroix, T. Lamb, A. Lancetov, M. Larsson, D. Le Pinvidic, S. Lederer, T. Lensch, D. Lenz, A. Leuschner, F. Levenhagen, Y. Li, J. Liebing, L. Lilje, T. Limberg, D. Lipka, B. List, J. Liu, S. Liu, B. Lorbeer, J. Lorkiewicz, H. H. Lu, F. Ludwig, K. Machau, W. Maciocha, C. Madec, C. Magueur, C. Maiano, I. Maksimova, K. Malcher, T. Maltezopoulos, E. Mamoshkina, B. Manschwetus, F. Marcellini, G. Marinkovic, T. Martinez, H. Martirosyan, W. Maschmann, M. Maslov, A. Matheisen, U. Mavric, J. Meißner, K. Meissner, M. Messerschmidt, N. Meyners, G. Michalski, P. Michelato, N. Mildner, M. Moe, F. Moglia, C. Mohr, S. Mohr, W. Möller, M. Mommerz, L. Monaco, C. Montiel, M. Moretti, I. Morozov, P. Morozov, and D. Mross, *Nat. Photonics* **14**, 391 (2020).

2. G. Geloni, E. Saldin, L. Samoylova, E. Schneidmiller, H. Sinn, T. Tschentscher, and M. Yurkov, New J. Phys. **12**, 035021 (2010).

3. G. Palmer, M. Kellert, J. Wang, M. Emons, U. Wegner, D. Kane, F. Pallas, T. Jezynski, S. Venkatesan, D. Rompotis, E. Brambrink, B. Monoszlai, M. Jiang, J. Meier, K. Kruse, M. Pergament, and M. J. Lederer, J. Synchrotron Radiat. **26**, 328 (2019).

4. S. Serkez, G. Geloni, S. Tomin, G. Feng, E. V. Gryzlova, A. N. Grum-Grzhimailo, and M. Meyer, J. Opt. **20**, 024005 (2018).

5. S. Pandey, R. Bean, T. Sato, I. Poudyal, J. Bielecki, J. C. Villarreal, O. Yefanov, V. Mariani, T. A. White, C. Kupitz, M. Hunter, M. H. Abdellatif, S. Bajt, V. Bondar, A. Echelmeier, D. Doppler, M. Emons, M. Frank, R. Fromme, Y. Gevorkov, G. Giovanetti, M. Jiang, D. Kim, Y. Kim, H. Kirkwood, A. Klimovskaia, J. Knoska, F. H. M. Koua, R. Letrun, S. Lisova, L. Maia, V. Mazalova, D. Meza, T. Michelat, A. Ourmazd, G. Palmer, M. Ramilli, R. Schubert, P. Schwander, A. Silenzi, J. Sztuk-Dambietz, A. Tolstikova, H. N. Chapman, A. Ros, A. Barty, P. Fromme, A. P. Mancuso, and M. Schmidt, Nat. Methods **17**, 73 (2020).

6. M. K. Czwalinna, R. Boll, H. Kirkwood, J. Koliyadu, J. Kral, B. Lautenschlager, R. Letrun, J. Liu, J. Müller, F. Pallas, D. E. Rivas, T. Sato, H. Schlarb, S. Schulz, and B. Steffen, in *Proceedings of International Particle Accelerator Conference* (JACoW Publishing, 2021), p. 3714.

7. M. K. Czwalinna, M. Felber, M. Fenner, C. Gerth, T. Kozak, T. Lamb, B. Lautenschlager, F. Ludwig, U. Mavrič, J. Müller, S. Pfeiffer, H. Schlarb, C. Schmidt, C. Sydlo, M. Titberidze, F. Zummack, and S. Schulz, in *39th International Free-Electron Laser Conference* (JACoW Publishing, 2019), p. 318.

8. B. Lautenschlager, M. K. Czwalinna, J. Kral, J. Müller, S. Pfeiffer, H. Schlarb, C. Schmidt, S. Schulz, M. Schütte, and B. Steffen, in *40th International Free Electron Laser Conference* (JACoW Publishing, 2023), p. 421.

9. H. Schlarb, M. K. Czwalinna, and S. Schulz, in *67th ICFA Advanced Beam Dynamics Workshop on Future Light Sources* (JACoW Publishing, 2023), paper WE3D.

10. M. S. Longuet-Higgins, Philos. Trans. R. Soc. London A **243**, 1 (1950).

11. D. Becker, L. Cristiano, J. Peikert, T. Kruse, F. Dethof, C. Hadziioannou, and T. Meier, J. Geophys. Res. Solid Earth **125**, e2020JB019770 (2020).

12. F. Ardhuin, L. Gualtieri, and E. Stutzmann, Geophys. Res. Lett. **42**, 765 (2015).

13. T. Parker, S. Shatalin, and M. Farhadiroushan, First Break **32**, 61 (2014).

14. Y. Li, M. Karrenbach, and J. Ajo-Franklin, *Distributed Acoustic Sensing in Geophysics: Methods and Applications*, Vol. 268 (John Wiley & Sons, 2022).

15. http://wave-hamburg.eu/.

16. E. Sidenko, K. Tertyshnikov, M. Lebedev, and R. Pevzner, Geophysics **87**, D111 (2022).

17. A. Agababyan, G. Asova, G. Dimitrov, G. Grygiel, B. Fominykh, O. Hensler, R. Kammering, L. Petrosyan, K. Rehlich, V. Rybnikov, G. Trowitzsch, M. Winde, and T. Wilksen, in *15th IEEE NPSS Real Time Conference* (IEEE, 2007), p. 1.

18. H. L. Tolman. "User manual and system documentation of WAVEWATCH III™ version 3.14", Technical Note (US National Oceanic and Atmospheric Administration, 2009).

19. F. Bi, J. Song, K. Wu, and Y. Xu, Acta Oceanol. Sin. **34**, 43 (2015).

20. E. Stutzmann, M. Schimmel, G. Patau, and A. Maggi, Geochemistry Geophys. Geosyst. **10**, Q11004 (2009).

21. C. Juretzek and C. Hadziioannou, J. Geophys. Res. Solid Earth **121**, 6741 (2016).

22. M. R. Guy, J. M. Patton, J. Fee, M. Hearne, E. Martinez, D. Ketchum, C. Worden, V. Quitoriano, E. Hunter, G. Smoczyk, and S. Schwarz, "National Earthquake Information Center systems overview and integration", Technical Report (US Geological Survey, 2015).

23. https://meteostat.net/en/place/de/helgoland?s=10015&t=2024-01-05/2024-01-12.

24. E. M. Rathje, N. A. Abrahamson, and J. D. Bray, J. Geotechn. Geoenviron. Eng. **124**, 150 (1998).

25. P. M. Shearer, *Introduction to Seismology* (Cambridge University Press, 2019).

26. https://github.com/cambecc/earth.

27. T. Forbriger, N. Karamzadeh, J. Azzola, E. Gaucher, R. Widmer-Schnidrig, and A. Rietbrock, arXiv:2408.01151 (2024).

28. L Astiz, in *29th General Assembly of the International Association of Seismology and Physics of the Earth's Interior* (IASPEI, 1997).